

# Room-Temperature Quantitative Quantum Sensing of Lithium Ions with a Radical-Embedded Metal–Organic Framework

Lei Sun,\* Luming Yang, Jin-Hu Dou, Jian Li, Grigorii Skorupskii, Michael Mardini, Kong Ooi Tan, Tianyang Chen, Chenyue Sun, Julius J. Oppenheim, Robert G. Griffin, Mircea Dincă,\* and Tijana Rajh\*



Cite This: <https://doi.org/10.1021/jacs.2c07692>



Read Online

ACCESS |



Metrics & More



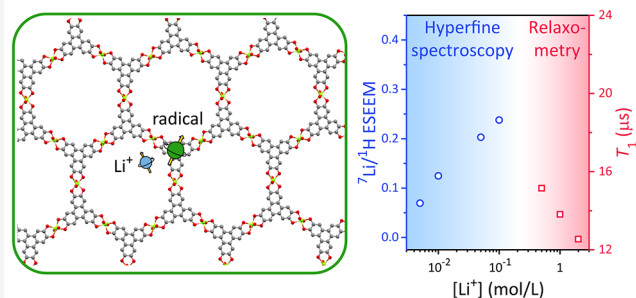
Article Recommendations



Supporting Information

**ABSTRACT:** Recent advancements in quantum sensing have sparked transformative detection technologies with high sensitivity, precision, and spatial resolution. Owing to their atomic-level tunability, molecular qubits and ensembles thereof are promising candidates for sensing chemical analytes. Here, we show quantum sensing of lithium ions in solution at room temperature with an ensemble of organic radicals integrated in a microporous metal–organic framework (MOF). The organic radicals exhibit electron spin coherence and microwave addressability at room temperature, thus behaving as qubits. The high surface area of the MOF promotes accessibility of the guest analytes to the organic qubits, enabling unambiguous identification of lithium ions and quantitative measurement of their concentration through relaxometric and hyperfine spectroscopic methods based on electron paramagnetic resonance (EPR) spectroscopy. The sensing principle presented in this work is applicable to other metal ions with nonzero nuclear spin.

## Room-Temperature Quantitative Quantum Sensing of Li<sup>+</sup>



## INTRODUCTION

Quantum sensing exploits quantum phenomena to measure physical quantities including magnetic field, electric field, temperature, pressure, pH, time, and frequency, among others.<sup>1</sup> The ability to coherently address single qubits and qubit ensembles has sparked revolutionary sensing technologies with nanoscale spatial resolution as well as ultrahigh sensitivity and precision,<sup>1</sup> enabling atomic-level magnetic resonance imaging,<sup>2</sup> single-molecule magnetometry,<sup>3,4</sup> and magnetic imaging of living cells.<sup>5</sup>

Despite these advances and applications, an outstanding open challenge is to apply quantum sensing for quantifying chemical analytes in ambient conditions, which could be instrumental for a range of technologies spanning biological systems and energy storage devices.<sup>6–8</sup> The vast majority of qubits, including superconducting circuits,<sup>9</sup> semiconductor quantum dots,<sup>10</sup> trapped ions,<sup>11</sup> and neutral atoms,<sup>12</sup> have limited application in ambient conditions because they typically require cryogenic temperature and/or strictly controlled environments. Although qubits based on solid-state defects such as nitrogen–vacancy (NV) centers in diamond can operate at room temperature and have been used to detect chemical analytes through  $T_1$  relaxometry<sup>13</sup> and magnetic resonance spectroscopy,<sup>3,4,14</sup> they are typically buried inside the insulating solid, preventing close contact and strong interaction with chemicals.<sup>4,6</sup> Furthermore, solid-state defect qubits most often lack designability and tunability that are

critical for selective and simultaneous sensing of multiple species.<sup>6</sup> To this end, molecular qubits, a class of paramagnetic molecules that exhibit electron spin coherence,<sup>15</sup> are promising alternative candidates that can be modified with selective and strong binding sites for chemical analytes<sup>16</sup> and, in certain cases, can operate at room temperature.<sup>17–22</sup> Integrating solid-state materials with molecular qubits can therefore create a powerful new platform for quantum sensing.

Recent research on molecular qubits based on transition-metal or lanthanide electron spin centers<sup>15,23–25</sup> has revealed design rules for achieving millisecond phase memory time<sup>26,27</sup> or optical addressability<sup>28</sup> at cryogenic temperature and has established strategies to construct spatially ordered molecular qubit arrays.<sup>29,30</sup> Nonetheless, except for a small number of examples with Cu(II), V(IV), or Y(II) as spin centers,<sup>17–22</sup> most metal-based molecular qubits do not operate at room temperature due to fast spin–lattice relaxation induced by spin–orbit couplings at the metal sites.<sup>20,31,32</sup> In this regard, organic radicals with unpaired electron spins residing on light atoms with negligible spin–orbit coupling, such as carbon,

Received: July 22, 2022



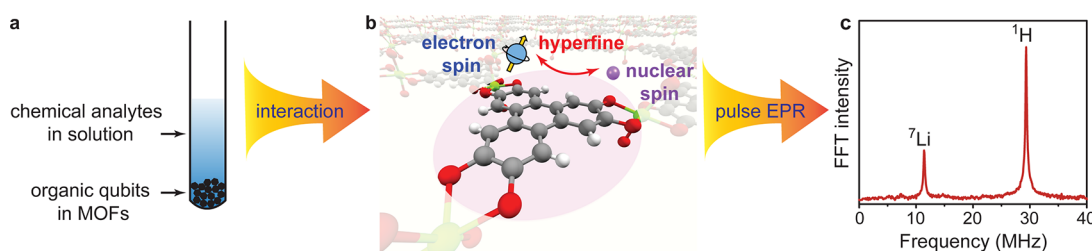


**Figure 1.** Room-temperature quantum sensing using organic radicals in MOFs. (a) MOF particles with organic qubits are suspended in a solution containing the desired analyte, in this case a solution of  $\text{LiClO}_4$  in THF. (b) Chemical analytes are adsorbed into the MOF and interact with the embedded radicals through hyperfine coupling. The pink circle indicates that the electron spin delocalizes throughout the HOTP ligand. (c) Nuclei interacting with the radical qubit can be identified based on the hyperfine spectrum, which further allows quantification of the chemical analytes.

nitrogen, and oxygen, are promising alternatives. When dilute, these can maintain spin coherence at room temperature with microsecond-scale phase memory time.<sup>31,33</sup> Although these properties have enabled wide use of organic radicals as spin labels in biological systems<sup>34</sup> and as polarizing agents in dynamic nuclear polarization,<sup>35</sup> organic radicals remain unexplored for quantum sensing.

One powerful approach for achieving room-temperature quantitative sensing of chemical analytes is relaxometry, which probes spin relaxation to relay information about concentration.<sup>36</sup> Although widely used in magnetic resonance imaging and recently demonstrated for quantum sensors based on NV centers in diamond,<sup>13</sup> this technique still has limited application in chemical identification and simultaneous sensing of multiple analytes. A related, but potentially more versatile approach is the detection of nuclear hyperfine fields stemming from the coupling between an electron spin qubit and nuclear spins in its environment. This can be achieved by hyperfine spectroscopy, which can identify the nuclear species and possibly characterize coupling strengths (Figure 1c).<sup>37</sup> Because hyperfine fields are typically limited to short distances, close contact between the electron spin qubit and the target nuclei is a key requirement for implementing this sensing scheme.<sup>6</sup>

Because of their high surface area, MOFs are ideal hosts for molecular qubits to promote qubit–analyte accessibility. MOFs are porous ordered solids composed of inorganic and organic molecular building blocks.<sup>38</sup> They typically contain nanoscale or subnanoscale pores that have enabled their use in traditional sensing applications.<sup>39,40</sup> Previously, it has been shown that electron spins in microporous zeolites and MOFs can be used to detect guest species by hyperfine spectroscopy, but these demonstrations were performed at cryogenic temperatures (below 10 K) due to the limitation of electron spin coherence and/or sensitivity.<sup>41–43</sup> Here, we seek to incorporate organic radicals into the MOF backbone to enable room-temperature operability while preserving pore accessibility, leading to close radical–analyte contacts through adsorption (Figure 1b). In addition, MOFs can be elaborated as inert and insoluble solids for either liquid or solution phase analytes (Figure 1a). This suppresses radical tumbling typical for liquids<sup>31</sup> and improves detection sensitivity by concentrating the solid-embedded radicals to an extent that is unreachable with soluble species.

A material that showcases these concepts is  $\{[\text{Mg}(\text{H}_2\text{O})_2]_3\text{HOTP}_2\}\{[\text{Mg}(\text{H}_2\text{O})_4]_3\text{HOTP}_2\}_2$  (MgHOTP, HOTP = 2,3,6,7,10,11-hexaoxytriphenylene), a new MOF bearing closed-shell metal ions, nanoscale pores, and organic radicals as the only paramagnetic centers (Figure 1). Besides avoiding electron–electron relaxation pathways, diamagnetic

$\text{Mg}^{2+}$  ions are ideal for this application because the high natural abundance of  $^{24}\text{Mg}$  (90%), an isotope with zero nuclear spin, also minimizes electron–nucleus relaxation. The tritopic ligand 2,3,6,7,10,11-hexahydroxytriphenylene (HOTP) is a common building block in two-dimensional (2D) porous MOFs,<sup>44</sup> whose spontaneous oxidation generates a radical.<sup>45,46</sup> Using EPR spectroscopy, we demonstrate that the radicals in MgHOTP behave as electron spin qubits, whose quantum states can be partially polarized by an external magnetic field, manipulated by microwave pulses, and read out through electron spin echo schemes. We further demonstrate quantitative detection of lithium ions ( $\text{Li}^+$ ) in solution at room temperature using MgHOTP qubits with relaxometry and hyperfine spectroscopy.

## RESULTS AND DISCUSSION

**Synthesis and Structure of MgHOTP.** A solvothermal aerobic reaction between magnesium acetate and HOTP in a mixture of water and dimethyl sulfoxide yields MgHOTP as a navy-black microcrystalline powder composed of hexagonal rodlike single crystals, with the longest dimension ranging from 0.5 to 13  $\mu\text{m}$  (Figures S1–S3). The single-crystal structure of MgHOTP was solved through a combined refinement of continuous rotation electron diffraction (cRED) and synchrotron powder X-ray diffraction (PXRD) data (Figures S4–S7, Table S1).<sup>47,48</sup> It consists of two components: extended 2D honeycomb sheets with the formula  $[\text{Mg}(\text{H}_2\text{O})_2]_3\text{HOTP}_2$  (Figure 2a,c) and isolated molecular clusters with the formula  $[\text{Mg}(\text{H}_2\text{O})_4]_3\text{HOTP}$  (Figure 2b,d; see discussion about charge assignment in the Supporting Information). The molecular clusters sit in-between neighboring sheets and manifest alternating interlayer spacing of 3.2 and 3.5 Å (Figure 2e); HOTP ligands in the clusters and those within the sheets are eclipsed with a rotation (Figure 2b). Cryogenic electron microscopy (cryo-EM) and fast Fourier transform (FFT) analysis of MgHOTP corroborate the structure obtained by cRED and PXRD (Figure 2f–h). The eclipsed stacking in MgHOTP leads to one-dimensional (1D) pores with a diameter of  $\sim 1.4$  nm (Figure 2a,b). This structure remains stable in ambient conditions, in solvents including tetrahydrofuran (THF) and water, and upon activation under vacuum at 60 °C (Figures S1 and S4). Activation produces a desolvated framework that exhibits a Brunauer–Emmet–Teller surface area of 481  $\text{m}^2/\text{g}$ , as determined by  $\text{N}_2$  adsorption at 77 K (Figures S8 and S9). Critically, these pores provide sufficiently large apertures for solvated metal ions to enter and interact with the HOTP radicals.

**Organic Electron Spin Qubits in MgHOTP.** There are two crystallographically distinguishable HOTP ligands in the

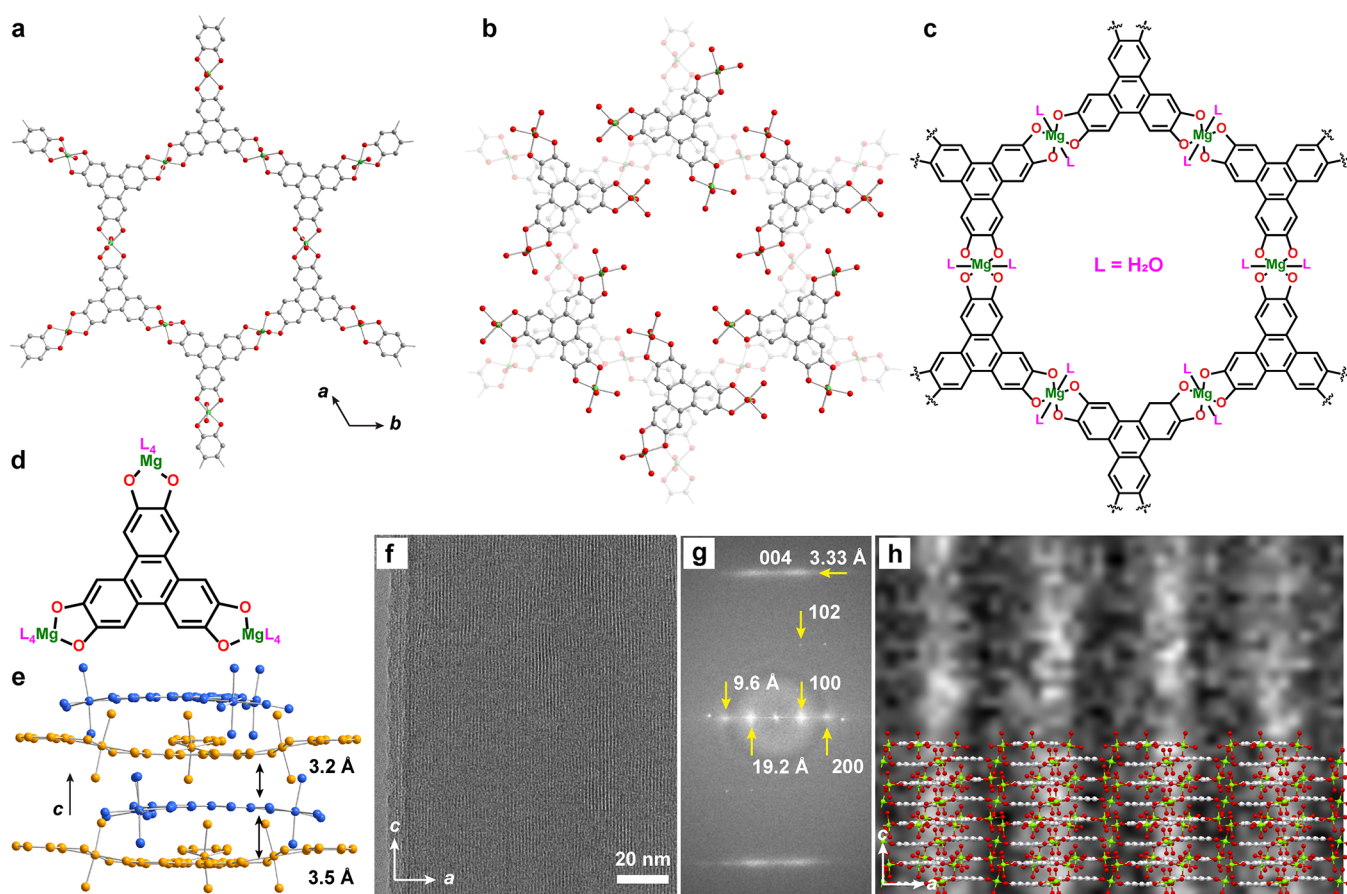


**Figure 2.** Single-crystal structure of MgHOTP derived from cRED and synchrotron PXRD. (a, b) Structural representation of single and double layers of MgHOTP viewed down the crystallographic *c*-axis, with (b) depicting the rotated eclipsed stacking between the clusters and the sheets. Green, red, and gray spheres represent Mg, O, and C atoms, respectively. H atoms are omitted for clarity. (c, d) Chemical structures of a portion of the  $[\text{Mg}(\text{H}_2\text{O})_2]_3\text{HOTP}_2$  sheet and one  $[\text{Mg}(\text{H}_2\text{O})_4]_3\text{HOTP}$  cluster, respectively. (e) View parallel to the crystallographic *ab*-plane, showing the deviation from planarity in the sheets (yellow) and the clusters (blue), as well as the two distinct interplanar distances. (f) Cryo-EM image of MgHOTP. (g) FFT of (f). (h) High-magnification micrograph from (f), with visible lattice fringes. High-contrast fringes perpendicular to the pore walls are spaced at 19.2 Å. They are overlaid with a structural model of MgHOTP showing the fringes that match well with the *d*-spacing along the crystallographic *a*-axis.

two structural components of MgHOTP. Each HOTP-centered radical may display one of three EPR-active oxidation states ( $\text{HOTP}^-$ ,  $\text{HOTP}^{3-}$ ,  $\text{HOTP}^{5-}$ ).<sup>49</sup> To probe these organic radicals, we performed continuous-wave (CW) and pulse EPR measurements on MgHOTP crystallites at room temperature (296 K). The X-band (9–10 GHz) CW EPR spectrum displays a single resonance peak at  $g = 2.00373$  with a Dysonian line shape and a line width of 0.33 mT (Figure 3a). The D-band (140 GHz) echo-detected field sweep (EDFS) spectrum further revealed  $g$  anisotropy values  $g_{\parallel} = 2.00221$  and  $g_{\perp} = 2.00497$  with anisotropic line broadening (Figure S10). These  $g$  values are typical for phenoxyl radicals.<sup>45</sup> Quantitative CW EPR analysis revealed that 1–2% of HOTP ligands contain a radical (Figure S11, Tables S2 and S3), corresponding to an electron spin concentration between  $2 \times 10^{-2}$  and  $4 \times 10^{-2}$  mol/L. Note that saturated solutions of the free-ligand HHTP in typical organic solvents such as THF do not show observable CW or pulse EPR signals. The relatively high radical concentration on HOTP is thus available only by integrating this ligand within the MOF.

Notably, only one type of spin center can be resolved even at the D band. The absence of other species infers the delocalized nature of the radical electron spins in MgHOTP. On the one hand, the HOTP-based radical is expected to be delocalized

within each HOTP unit over the triphenylene core and the oxygen atoms, as suggested by previous computational studies on HHTP and related trimetallic clusters.<sup>49</sup> On the other hand, electrical characterization of other HOTP-based MOFs and analogues further revealed that electrons can hop between different HOTP moieties along the out-of-plane direction.<sup>44,47,50</sup> Such intra-HOTP and inter-HOTP electron delocalization is likely facilitated by in-plane  $\pi$ -conjugation and out-of-plane  $\pi$ - $\pi$  stacking interactions, respectively.<sup>47</sup> Because of such delocalization, the radicals residing on different structural components and with different oxidation states may not be discernible; accordingly, their contribution to the quantum sensing performance should be taken as an ensemble.

Pulse EPR characterization provided key evidence in testing qubit-type behavior of HOTP radicals. Appropriate microwave pulses can orient electron spin qubits on arbitrary positions, contrasting with electron spin bits used in regular spintronic devices, which exclusively use binary positions for information processing.<sup>23,24</sup> When electron spins behave like qubits, under magnetic field, they satisfy the Rabi relationship  $\hbar\omega_{\text{Rabi}} = g\mu_{\text{B}}SB_1$ , where  $\hbar$  is the reduced Planck constant,  $\omega_{\text{Rabi}}$  is the Rabi frequency,  $\mu_{\text{B}}$  is the Bohr magneton, and  $B_1$  is the microwave magnetic field strength. Importantly, under micro-

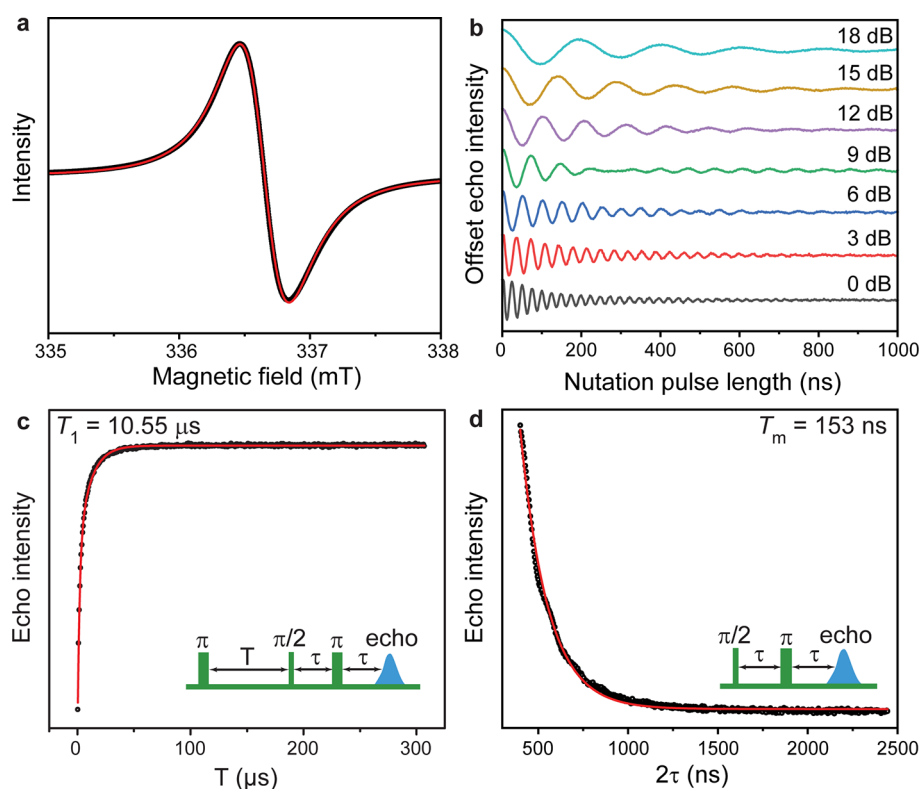


**Figure 3.** Organic electron spin qubits in dry powders of MgHOTP at room temperature. (a) CW EPR spectrum. The red line is the fitting curve obtained from Dysonian line shape using  $S = 1/2$  and  $g = 2.00373$ . (b) Nutation experiments at various microwave attenuations. (c) Inversion recovery measurement of  $T_1$ . The red line is a biexponential decay fitting curve. Inset: pulse sequence for the inversion recovery experiment. (d) Hahn echo decay measurement of  $T_m$ . The red line is a monoexponential decay fitting curve. Inset: pulse sequence for the Hahn echo decay experiment. These data were collected with X-band EPR at 296 K.

wave pulses of various power and length, MgHOTP exhibits oscillations of spin orientations with frequencies  $\omega_{\text{Rabi}}$  that are linearly dependent on  $B_1$  (Figures 3b and S12), providing key evidence that radicals in MgHOTP are suitable for single-qubit quantum gate operations.<sup>24</sup> More practically, an electron spin qubit must also possess long spin–lattice relaxation time ( $T_1$ ) and phase memory time ( $T_m$ ) to ensure sufficient duration of its polarization and coherence.<sup>31,51</sup> To measure  $T_1$  and  $T_m$ , we employed inversion recovery and Hahn echo decay pulse sequences, respectively, on dry powders of MgHOTP. Depending on the synthetic conditions of each batch of MgHOTP, these measurements gave room-temperature values of  $T_1$  ranging from 9.48 to 21.34  $\mu\text{s}$  and  $T_m$  ranging from 153 to 239 ns at 296 K (Figures 3c,d and S13), qualifying MgHOTP as a potential candidate for quantum sensing of chemical analytes under ambient conditions.

**Quantitative Quantum Sensing of Lithium Ions by MgHOTP.** To demonstrate the utility of MgHOTP in quantum sensing, we targeted the detection of  $\text{Li}^+$  ions because of their important role in energy-related and biological applications.<sup>8</sup> Additionally,  $\text{Li}^+$  should show affinity toward the oxygen atoms lining the pores of MgHOTP,<sup>52</sup> and the major Li isotope,  $^7\text{Li}$  (92.4% natural abundance), has a unique nuclear Larmor frequency, which minimizes potential interference from other nuclei. Treatment of MgHOTP powders with solutions of  $\text{LiClO}_4$  in THF leads to incorporation of  $\text{Li}^+$  within the MOF without significantly affecting its structural integrity (Figure S4), the  $g$  factor of the organic radical, or its qubit behavior (Figures S12 and S14, Table S4). However,  $T_1$  and  $T_m$  changed when the concentration of  $\text{Li}^+$  ( $[\text{Li}^+]$ ) ranged

between 0.1 and 2.0 mol/L, giving rise to relaxometric detection in this range. For instance, in a given MgHOTP batch whose dry powder exhibits  $T_1 = 10.55 \mu\text{s}$  and  $T_m = 153 \text{ ns}$  (Figure 3c,d), when  $[\text{Li}^+] < 0.1 \text{ mol/L}$ , both  $T_1$  and  $T_m$  remain relatively constant ( $T_1 = 20\text{--}21 \mu\text{s}$ ,  $T_m = 190\text{--}200 \text{ ns}$ ), but increasing  $[\text{Li}^+]$  reduces both  $T_1$  and  $T_m$  significantly, reaching  $T_1 = 12.55 \mu\text{s}$  and  $T_m = 169 \text{ ns}$  for  $[\text{Li}^+] = 2 \text{ mol/L}$  (Figures 4a and S15, Table S5). Moreover,  $^6\text{Li}$  solid-state nuclear magnetic resonance (NMR) spectroscopic studies showed a significant reduction of the nuclear  $T_1$  of  $^6\text{Li}^+$  upon incorporation into MgHOTP (Figures S16 and S17). These observations point toward radical– $\text{Li}^+$  hyperfine interaction, indicating close contact between  $\text{Li}^+$  in the MgHOTP pores and the negatively charged atomic sites of the delocalized radicals as a result of Coulombic attraction. This hypothesis is corroborated by previous computational and crystallographic studies on alkali metal complexes with HHTP and catecholate derivatives.<sup>52–56</sup>

Interrogating the radical– $\text{Li}^+$  hyperfine interaction can provide much higher sensitivity for  $\text{Li}^+$  sensing. This interaction can be probed by combination-peak electron spin echo envelope modulation (CP-ESEEM) spectroscopy,<sup>37,57</sup> which balances sensitivity, resolution, and acquisition time (Figure S18) by employing a four-pulse sequence ( $\pi/2\text{--}\tau\text{--}\pi/2\text{--}T\text{--}\pi\text{--}T\text{--}\pi/2\text{--}\tau\text{--}\text{echo}$ ), with the nuclear spin precession modulating electron spin echo decay during evolution times  $T$  (Figure 4b). In the weak-coupling regime, where the hyperfine constant is much smaller than the nuclear Larmor frequency ( $\omega_1$ ), as is the case for MgHOTP radical– $^7\text{Li}$  and radical– $^1\text{H}$  hyperfine interactions revealed by hyperfine sublevel correla-

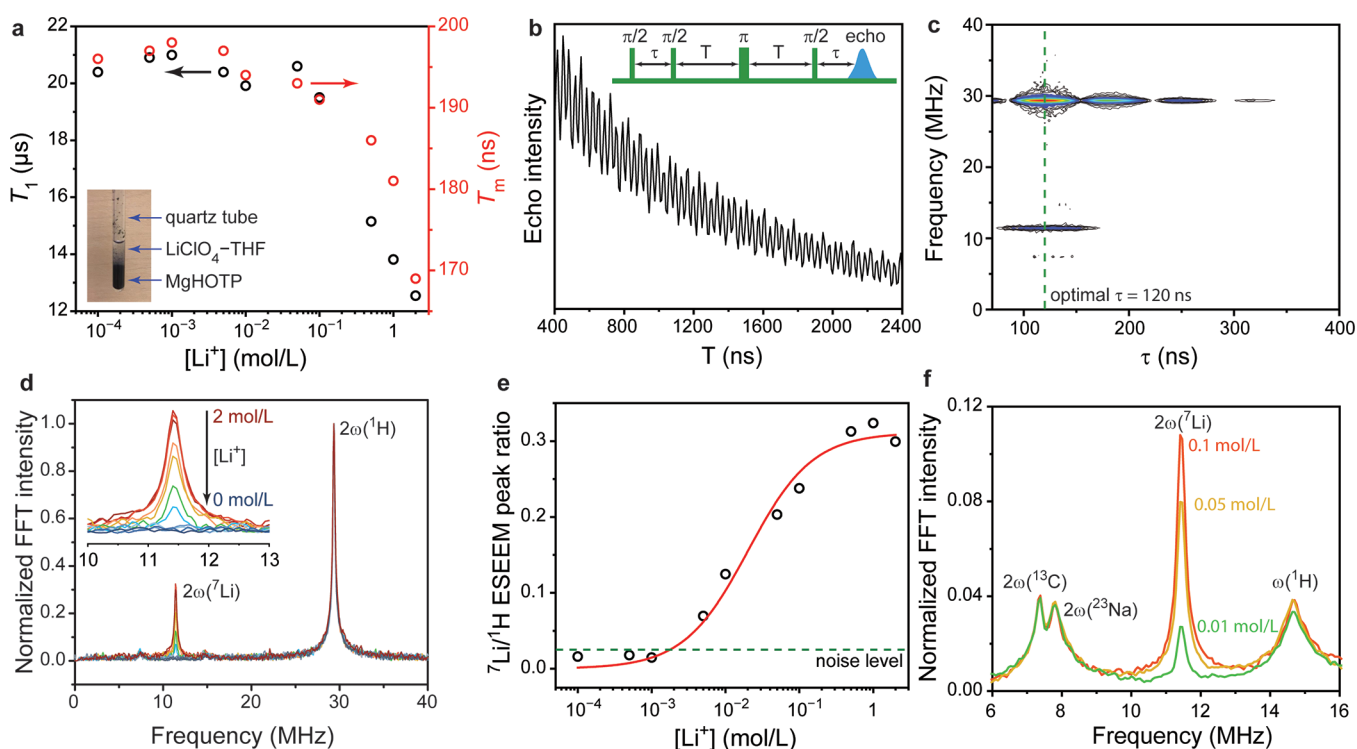


**Figure 4.** Quantitative sensing of  $\text{Li}^+$  in THF solution by MgHOTP at room temperature. (a)  $T_1$  and  $T_m$  of MgHOTP in THF solutions of  $\text{LiClO}_4$  with various  $[\text{Li}^+]$ . Inset: picture of a sample for the EPR measurement. (b) Portion of a time-domain CP-ESEEM spectrum of MgHOTP in a THF solution of  $\text{LiClO}_4$  where  $[\text{Li}^+] = 2.0$  mol/L. This measurement takes  $\sim 40$  min to gain high signal-to-noise ratio. Inset: pulse sequence of CP-ESEEM. (c) 2D spectrum of CP-ESEEM collected with various  $\tau$  values. (d) Frequency-domain CP-ESEEM spectra of MgHOTP in THF solutions of  $\text{LiClO}_4$  with various  $[\text{Li}^+]$ . The spectra were normalized to the  $2\omega(^1\text{H})$  peaks. Inset: zoom-in view on the  $2\omega(^7\text{Li})$  peaks. (e) Relationship between  $2\omega(^7\text{Li})/2\omega(^1\text{H})$  ESEEM peak ratio and  $[\text{Li}^+]$ . The former was calculated by dividing the maximum of the  $2\omega(^7\text{Li})$  peak with the maximum of the  $2\omega(^1\text{H})$  peak in each spectrum. Red curve represents fit of the data to the Langmuir adsorption model. Green dashed line represents the noise level estimated based on the spectrum of MgHOTP in pure THF. (f) Frequency-domain CP-ESEEM spectra of MgHOTP in THF solutions with 0.1 mol/L  $\text{NaClO}_4$  and various concentrations of  $\text{LiClO}_4$ . The spectra were normalized to the  $2\omega(^1\text{H})$  peak, which is not shown for clarity.

tion (HYSCORE) spectroscopic studies (Figures S19 and S20), the frequency-domain CP-ESEEM spectrum displays peaks at  $2\omega_1$  of the hyperfine nuclei.<sup>37</sup> Therefore, CP-ESEEM can serve as a decisive technique for the detection of various elements,  $^7\text{Li}$  and  $^1\text{H}$  in this case, that bear distinguishing Larmor frequencies.

The X-band CP-ESEEM spectrum of MgHOTP soaked in a THF solution with  $[\text{Li}^+] = 2$  mol/L displays two peaks at 11.41 and 29.34 MHz under a field of 344.53 mT, corresponding to  $2\omega_1$  of  $^7\text{Li}$  and  $^1\text{H}$ , respectively (Figure 4d). These peaks reflect the modulation of the HOTP electron spin by the nuclear spins of  $^7\text{Li}$  and  $^1\text{H}$  in the subnanometer proximity. They decisively identify  $^7\text{Li}$  and  $^1\text{H}$  in the environment surrounding HOTP. The  $^1\text{H}$  peak relates to MOF components or guest solvent molecules, as also confirmed by control CP-ESEEM studies of MgHOTP in deuterated solvents (Figures S21–S23). In contrast, the  $^7\text{Li}$  peak unambiguously confirms that MgHOTP behaves as a quantum sensor for  $\text{Li}^+$  at room temperature. The absence of  $^{35}\text{Cl}$  and  $^{37}\text{Cl}$  signals in CP-ESEEM spectra suggests negligible interaction between the MgHOTP qubits and  $\text{ClO}_4^-$ , likely due to Coulombic repulsion between the anions and the oxygen-rich pore surface of the framework. Indeed, CP-ESEEM signals from anions are also absent when employing other  $\text{Li}^+$  salts such as  $\text{LiCl}$  and  $\text{LiBr}$  (Figure S24), demonstrating the selectivity of MgHOTP toward cations.

Notably, CP-ESEEM with MgHOTP enables quantitative detection of even lower concentrations of  $\text{Li}^+$  because the ESEEM signal from  $^7\text{Li}$  can be referenced to that of an internal standard, here  $^1\text{H}$  (see theoretical analysis in the Supporting Information).<sup>58,59</sup> We took advantage of the narrow line width of MgHOTP (Figures 3a and S25)<sup>51</sup> and adopted an optimal CP-ESEEM delay time  $\tau = 120$  ns, which gives maximum modulation depth from  $^7\text{Li}$  (Figures 4c and S26–S28). With these parameters, all CP-ESEEM measurements display  $^1\text{H}$  peaks with the same line shape for any  $[\text{Li}^+]$  in the range  $1 \times 10^{-4}$ – $2$  mol/L (Figure 4d), showing minimal influence of  $^7\text{Li}$  nuclear spins on the radical– $^1\text{H}$  interactions. For  $[\text{Li}^+] \geq 5 \times 10^{-3}$  mol/L, the relative peak intensity of  $^7\text{Li}$  increases sigmoidally with  $\log[\text{Li}^+]$ , approaching a plateau above 0.5 mol/L (Figures 4e, S29, and S30, Tables S6–S8).

This relationship fits well to the Langmuir adsorption model,<sup>60</sup> which leads to the following correlation with the ESEEM intensity (see detailed discussion in the Supporting Information):

$$\frac{I_{7\text{Li}}}{I_{1\text{H}}} = c_k \frac{K_{\text{eq}}[\text{Li}^+]}{1 + K_{\text{eq}}[\text{Li}^+]}$$

Here,  $I_{7\text{Li}}$  and  $I_{1\text{H}}$  represent the ESEEM intensity of  $^7\text{Li}$  and  $^1\text{H}$ , respectively,  $c_k$  is a prefactor, and  $K_{\text{eq}}$  represents the equilibrium adsorption constant. The Langmuir adsorption model describes monolayer physical adsorption on a surface. It

suggests that sensing with MgHOTP is reserved to  $\text{Li}^+$  ions proximal to the pore surface, as would be expected given the fast decay of the radical- $^7\text{Li}$  hyperfine interaction with distance. Interestingly, the Langmuir behavior provides thermodynamic data that calibrate the strength of  $\text{Li}^+$  adsorption onto MgHOTP: fitting the data to the above equation gives  $K_{\text{eq}} = 49.5 \pm 10.2$  L/mol, consistent with a weak  $\text{Li}^+$ -MOF interaction.<sup>61</sup> Altogether, these results demonstrate that using CP-ESEEM with MgHOTP enables quantitative sensing of  $\text{Li}^+$  ions in the range  $5 \times 10^{-3}$ –0.5 mol/L under ambient conditions, a 2 orders of magnitude improvement over relaxometry. CP-ESEEM and relaxometry are nevertheless complementary: their combination enables an effective quantum sensing range of  $5 \times 10^{-3}$ –2 mol/L.

Crucially, the principles and methods above can be extended to the detection of other metal ions with nonzero nuclear spin and, by extension, should allow simultaneous detection of multiple metal ions that display distinguishable Larmor frequencies. We demonstrated this concept by using a sample of MgHOTP soaked in a THF solution of 0.1 mol/L  $\text{LiClO}_4$  and 0.1 mol/L  $\text{NaClO}_4$ . The CP-ESEEM spectrum of this sample at 296 K under a field of 344.64 mT revealed a peak at 7.81 MHz, the expected  $2\omega_1$  value for  $^{23}\text{Na}$ , in addition to peaks corresponding to  $^1\text{H}$ ,  $^7\text{Li}$ , and  $^{13}\text{C}$  (Figure 4f). The  $^{23}\text{Na}$  peak is significantly weaker than the  $^7\text{Li}$  peak, indicating weaker interaction between the framework and  $\text{Na}^+$ . With the  $2\omega_1$  of  $^1\text{H}$  peak as an internal reference, decreasing the  $[\text{Li}^+]$  to 0.05 and 0.01 mol/L while maintaining a constant  $[\text{Na}^+]$  caused concomitant decrease in the intensity of the  $^7\text{Li}$  peak without distinguishable changes in the  $^{23}\text{Na}$  peak (Figures 4f and S31, Table S9). These experiments demonstrate that MgHOTP is capable of simultaneous detection of  $\text{Li}^+$  and  $\text{Na}^+$  as well as quantification of  $\text{Li}^+$  in the presence of  $\text{Na}^+$ . Because sensitivity is a proxy for the binding strength of metal ions to MgHOTP, it is reasonable to expect that quantum sensing of divalent and multivalent metal ions would be even more efficient. Applying this methodology to multivalent ions and particular combinations of ions relevant for different technologies are obvious future extensions for this work.

**Potential Strategies to Improve Sensitivity.** The detection limit of  $\text{Li}^+$  ( $5 \times 10^{-3}$  mol/L) in our current setup highlights a conceptually novel detection technique but evidences limitations relative to optical or electrochemical sensing strategies,<sup>8,62</sup> which can quantify  $\text{Li}^+$  at the ppm level. Nonetheless, we expect the sensitivity would improve by optimizing material design and the quantum sensing protocols.

For instance, because the proportion of HOTP bearing radicals is merely 1–2% of all the ligands in MgHOTP, some of the  $\text{Li}^+$  interacting with MgHOTP remains undetectable. Thus, MOFs possessing higher concentrations of electron spins should give rise to significant sensitivity enhancement. However, as high spin concentration leads to stronger electron–electron dipolar interaction, which tends to reduce  $T_1$  and  $T_m$ ,<sup>31</sup> additional strategies, such as engineering the interspin distance, would have to be considered. This has been recently demonstrated in two MOFs containing copper porphyrin moieties, whose  $T_m$  remains nearly 50 ns at 10 K even with a high spin density of 0.30–0.35 mol/L.<sup>29,30</sup>

Further improvements may be observed by employing hyperfine spectroscopic methods based on dynamical decoupling.<sup>63,64</sup> Specifically, implementing a microwave pulse train as a frequency filter could suppress environmental magnetic

noise, improve coherence, and amplify the frequency corresponding to the analyte, thus enhancing sensitivity.<sup>1,64</sup>

## CONCLUSIONS AND OUTLOOK

The foregoing results convey the first demonstration of room-temperature quantum sensing using a MOF containing organic qubits. Relaxometry and CP-ESEEM combine to provide a wide range ( $5 \times 10^{-3}$ –2 mol/L) of sensitivity for  $\text{Li}^+$  ions as well as direct quantification of mixed ion solutions. This range is sufficient for quantitative detection in battery applications, where  $[\text{Li}^+]$  is typically at least millimolar.<sup>7,65</sup>

The demonstration of quantum sensing herein is limited to metal ions in weakly polar solvents with a relatively high concentration. Nonetheless, the methodology derived in this work suggests several clear directions that could offer additional breadth and utility. Functionalization of the MOF with specific metal-binding groups should further enhance selectivity for those ions,<sup>16</sup> while integration of positively charged radicals, e.g., tetrathiafulvalene radical cations,<sup>66</sup> may enable anion sensing. MOFs incorporating various binding sites may be applicable for simultaneous quantitative sensing of multiple species that possess nonzero nuclear spin. Moreover, adapting this methodology to lower frequency EPR measurements, where the microwave permittivity of strongly polar solvents is much higher,<sup>67</sup> should further broaden the utility of this quantum sensing protocol to biological and battery-related applications. Finally, the quantum sensing principles demonstrated herein are transferrable to other pulse EPR techniques. Ultimately, single ion/molecule sensitivity may be achieved by addressing single molecular electron spin qubits with optically or electrically detected magnetic resonance.<sup>28,68</sup>

## ASSOCIATED CONTENT

### Supporting Information

The Supporting Information is available free of charge at <https://pubs.acs.org/doi/10.1021/jacs.2c07692>.

Full descriptions of experimental methods, electron diffraction micrographs, PXRD patterns, thermogravimetric analysis,  $\text{N}_2$  adsorption isotherm, quantitative EPR analysis, solid-state nuclear magnetic resonance spectroscopic studies, pulse EPR characterization results, and theoretical analysis for quantitative sensing by CP-ESEEM (PDF)

### Accession Codes

CCDC 2103823 contains the supplementary crystallographic data for this paper. These data can be obtained free of charge via [www.ccdc.cam.ac.uk/data\\_request/cif](http://www.ccdc.cam.ac.uk/data_request/cif), or by emailing [data\\_request@ccdc.cam.ac.uk](mailto:data_request@ccdc.cam.ac.uk), or by contacting The Cambridge Crystallographic Data Centre, 12 Union Road, Cambridge CB2 1EZ, UK; fax: +44 1223 336033.

## AUTHOR INFORMATION

### Corresponding Authors

Lei Sun – Center for Nanoscale Materials, Argonne National Laboratory, Lemont, Illinois 60439, United States; [orcid.org/0000-0001-8467-6750](https://orcid.org/0000-0001-8467-6750); Email: [sunlei@westlake.edu.cn](mailto:sunlei@westlake.edu.cn)

Mircea Dincă – Department of Chemistry, Massachusetts Institute of Technology, Cambridge, Massachusetts 02139, United States; [orcid.org/0000-0002-1262-1264](https://orcid.org/0000-0002-1262-1264); Email: [mdinca@mit.edu](mailto:mdinca@mit.edu)

**Tijana Rajh** – Center for Nanoscale Materials, Argonne National Laboratory, Lemont, Illinois 60439, United States; The School for Molecular Sciences, Arizona State University, Tempe, Arizona 85281, United States; Email: [tijana.rajh@asu.edu](mailto:tijana.rajh@asu.edu)

## Authors

**Luming Yang** – Department of Chemistry, Massachusetts Institute of Technology, Cambridge, Massachusetts 02139, United States

**Jin-Hu Dou** – Department of Chemistry, Massachusetts Institute of Technology, Cambridge, Massachusetts 02139, United States; [orcid.org/0000-0002-6920-9051](https://orcid.org/0000-0002-6920-9051)

**Jian Li** – Department of Fibre and Polymer Technology, KTH Royal Institute of Technology, Stockholm 10044, Sweden

**Grigoriï Skorupskii** – Department of Chemistry, Massachusetts Institute of Technology, Cambridge, Massachusetts 02139, United States

**Michael Mardini** – Department of Chemistry and Francis Bitter Magnet Laboratory, Massachusetts Institute of Technology, Cambridge, Massachusetts 02139, United States

**Kong Ooi Tan** – Department of Chemistry and Francis Bitter Magnet Laboratory, Massachusetts Institute of Technology, Cambridge, Massachusetts 02139, United States; [orcid.org/0000-0002-3094-3398](https://orcid.org/0000-0002-3094-3398)

**Tianyang Chen** – Department of Chemistry, Massachusetts Institute of Technology, Cambridge, Massachusetts 02139, United States; [orcid.org/0000-0003-3142-8176](https://orcid.org/0000-0003-3142-8176)

**Chenyue Sun** – Department of Chemistry, Massachusetts Institute of Technology, Cambridge, Massachusetts 02139, United States

**Julius J. Oppenheim** – Department of Chemistry, Massachusetts Institute of Technology, Cambridge, Massachusetts 02139, United States

**Robert G. Griffin** – Department of Chemistry and Francis Bitter Magnet Laboratory, Massachusetts Institute of Technology, Cambridge, Massachusetts 02139, United States; [orcid.org/0000-0003-1589-832X](https://orcid.org/0000-0003-1589-832X)

Complete contact information is available at: <https://pubs.acs.org/10.1021/jacs.2c07692>

## Author Contributions

L.S. and L.Y. contributed equally to this work.

## Notes

The authors declare no competing financial interest.

## ACKNOWLEDGMENTS

This work was performed, in part, at the Center for Nanoscale Materials and used resources of Advanced Photon Source, both DOE Office of Science User Facilities, and was supported by Laboratory Directed Research and Development (LDRD) funding from Argonne National Laboratory, provided by the Director, Office of Science, of the U.S. Department of Energy under Contract DE-AC02-06CH11357. Work in the Dincă lab was supported by the Army Research Office (Award W911NF-21-1-0124). The cRED/MicroED data were collected at the Electron Microscopy Center (EMC), Department of Materials and Environmental Chemistry (MMK) in Stockholm University with the support of the Knut and Alice Wallenberg Foundation (KAW, 2012-0112) through the 3DEM-NATUR project. Work in the Griffin lab was supported by the National Institute of General Medical Sciences (GM132997 and

GM132079). We thank Dr. Walter Masefski for assistance in solid-state NMR measurements, Aimei Zhou for assistance in PXRD measurements, and Dr. Jenna L. Mancuso as well as Dr. Christopher H. Hendon for helpful discussions.

## REFERENCES

- (1) Degen, C. L.; Reinhard, F.; Cappellaro, P. Quantum sensing. *Rev. Mod. Phys.* **2017**, *89*, No. 035002.
- (2) Abobeih, M. H.; Randall, J.; Bradley, C. E.; Bartling, H. P.; Bakker, M. A.; Degen, M. J.; Markham, M.; Twitchen, D. J.; Taminiau, T. H. Atomic-scale imaging of a 27-nuclear-spin cluster using a quantum sensor. *Nature* **2019**, *576*, 411–415.
- (3) Shi, F.; Zhang, Q.; Wang, P.; Sun, H.; Wang, J.; Rong, X.; Chen, M.; Ju, C.; Reinhard, F.; Chen, H.; Wrachtrup, J.; Wang, J.; Du, J. Single-protein spin resonance spectroscopy under ambient conditions. *Science* **2015**, *347*, 1135–1138.
- (4) Lovchinsky, I.; Sushkov, A. O.; Urbach, E.; de Leon, N. P.; Choi, S.; De Greve, K.; Evans, R.; Gertner, R.; Bersin, E.; Müller, C.; McGuinness, L.; Jelezko, F.; Walsworth, R. L.; Park, H.; Lukin, M. D. Nuclear magnetic resonance detection and spectroscopy of single proteins using quantum logic. *Science* **2016**, *351*, 836–841.
- (5) Le Sage, D.; Arai, K.; Glenn, D. R.; DeVience, S. J.; Pham, L. M.; Rahn-Lee, L.; Lukin, M. D.; Yacoby, A.; Komeili, A.; Walsworth, R. L. Optical magnetic imaging of living cells. *Nature* **2013**, *496*, 486–489.
- (6) Yu, C.-J.; von Kugelgen, S.; Laorenza, D. W.; Freedman, D. E. A molecular approach to quantum sensing. *ACS Cent. Sci.* **2021**, *7*, 712–723.
- (7) Dutoit, C.-E.; Tang, M.; Gourier, D.; Tarascon, J.-M.; Vezin, H.; Salager, E. Monitoring metallic sub-micrometric lithium structures in Li-ion batteries by in situ electron paramagnetic resonance correlated spectroscopy and imaging. *Nat. Commun.* **2021**, *12*, 1410.
- (8) Villemin, E.; Raccurt, O. Optical lithium sensors. *Coord. Chem. Rev.* **2021**, *435*, 213801.
- (9) Blais, A.; Grimsmo, A. L.; Girvin, S. M.; Wallraff, A. Circuit quantum electrodynamics. *Rev. Mod. Phys.* **2021**, *93*, No. 025005.
- (10) Kloeffel, C.; Loss, D. Prospects for spin-based quantum computing in quantum dots. *Annu. Rev. Condens. Matter Phys.* **2013**, *4*, 51–81.
- (11) Bruzewicz, C. D.; Chiaverini, J.; McConnell, R.; Sage, J. M. Trapped-ion quantum computing: progress and challenges. *Appl. Phys. Rev.* **2019**, *6*, No. 021314.
- (12) Saffman, M. Quantum computing with atomic qubits and Rydberg interactions: progress and challenges. *J. Phys. B: At. Mol. Opt. Phys.* **2016**, *49*, 202001.
- (13) Sushkov, A. O.; Chisholm, N.; Lovchinsky, I.; Kubo, M.; Lo, P. K.; Bennett, S. D.; Hunger, D.; Akimov, A.; Walsworth, R. L.; Park, H.; Lukin, M. D. All-optical sensing of a single-molecule electron spin. *Nano Lett.* **2014**, *14*, 6443–6448.
- (14) Miller, B. S.; Bezing, L.; Gliddon, H. D.; Huang, D.; Dold, G.; Gray, E. R.; Heaney, J.; Dobson, P. J.; Nastouli, E.; Morton, J. J. L.; McKendry, R. A. Spin-Enhanced Nanodiamond Biosensing for Ultrasensitive Diagnostics. *Nature* **2020**, *587*, 588–593.
- (15) Wasielewski, M. R.; Forbes, M. D. E.; Frank, N. L.; Kowalski, K.; Scholes, G. D.; Yuen-Zhou, J.; Baldo, M. A.; Freedman, D. E.; Goldsmith, R. H.; Goodson, T., III; Kirk, M. L.; McCusker, J. K.; Ogilvie, J. P.; Shultz, D. A.; Stoll, S.; Whaley, K. B. Exploiting chemistry and molecular systems for quantum information science. *Nat. Rev. Chem.* **2020**, *4*, 490–504.
- (16) Yeung, M. C.-L.; Yam, V. W.-W. Luminescent cation sensors: from host–guest chemistry, supramolecular chemistry to reaction-based mechanisms. *Chem. Soc. Rev.* **2015**, *44*, 4192–4202.
- (17) Bader, K.; Dengler, D.; Lenz, S.; Endeward, B.; Jiang, S.-D.; Neugebauer, P.; van Slageren, J. Room temperature quantum coherence in a potential molecular qubit. *Nat. Commun.* **2014**, *5*, 5304.
- (18) Atzori, M.; Tesi, L.; Morra, E.; Chiesa, M.; Sorace, L.; Sessoli, R. Room-temperature quantum coherence and Rabi oscillations in

- vanadyl phthalocyanine: toward multifunctional molecular spin qubits. *J. Am. Chem. Soc.* **2016**, *138*, 2154–2157.
- (19) Yamabayashi, T.; Atzori, M.; Tesi, L.; Cosquer, G.; Santanni, F.; Boulon, M.-E.; Morra, E.; Benci, S.; Torre, R.; Chiesa, M.; Sorace, L.; Sessoli, R.; Yamashita, M. Scaling up electronic spin qubits into a three-dimensional metal–organic framework. *J. Am. Chem. Soc.* **2018**, *140*, 12090–12101.
- (20) Ariciu, A.-M.; Woen, D. H.; Huh, D. N.; Nodaraki, L. E.; Kostopoulos, A. K.; Goodwin, C. A. P.; Chilton, N. F.; McInnes, E. J. L.; Winpenny, R. E. P.; Evans, W. J.; Tuna, F. Engineering electronic structure to prolong relaxation times in molecular qubits by minimising orbital angular momentum. *Nat. Commun.* **2019**, *10*, 3330.
- (21) Urtizberea, A.; Natividad, E.; Alonso, P. J.; Pérez-Martínez, L.; Andrés, M. A.; Gascón, I.; Gimeno, I.; Luis, F.; Roubeau, O. Vanadyl spin qubit 2D arrays and their integration on superconducting resonators. *Mater. Horiz.* **2020**, *7*, 885–897.
- (22) Fataftah, M. S.; Krzyaniak, M. D.; Vlaisavljevich, B.; Wasielewski, M. R.; Zadrozny, J. M.; Freedman, D. E. Metal–ligand covalency enables room temperature molecular qubit candidates. *Chem. Sci.* **2019**, *10*, 6707–6714.
- (23) Gaita-Ariño, A.; Luis, F.; Hill, S.; Coronado, E. Molecular spins for quantum computation. *Nat. Chem.* **2019**, *11*, 301–309.
- (24) Atzori, M.; Sessoli, R. The second quantum revolution: role and challenges of molecular chemistry. *J. Am. Chem. Soc.* **2019**, *141*, 11339–11352.
- (25) Aromí, G.; Roubeau, O. Lanthanide Molecules for Spin-Based Quantum Technologies. In *Handbook on the Physics and Chemistry of Rare Earths*; Elsevier: 2019; Vol. 56, pp 1–54.
- (26) Zadrozny, J. M.; Niklas, J.; Poluektov, O. G.; Freedman, D. E. Millisecond coherence time in a tunable molecular electronic spin qubit. *ACS Cent. Sci.* **2015**, *1*, 488–492.
- (27) Dai, Y.; Fu, Y.; Shi, Z.; Qin, X.; Mu, S.; Wu, Y.; Su, J.-H.; Deng, Y.-F.; Qin, L.; Zhai, Y.-Q.; Zheng, Y.-Z.; Rong, X.; Du, J. Experimental protection of the spin coherence of a molecular qubit exceeding a millisecond. *Chin. Phys. Lett.* **2021**, *38*, No. 030303.
- (28) Bayliss, S. L.; Laorenza, D. W.; Mintun, P. J.; Kovos, B. D.; Freedman, D. E.; Awschalom, D. D. Optically addressable molecular spins for quantum information processing. *Science* **2020**, *370*, 1309–1312.
- (29) Yu, C.-J.; Krzyaniak, M. D.; Fataftah, M. S.; Wasielewski, M. R.; Freedman, D. E. A concentrated array of copper porphyrin candidate qubits. *Chem. Sci.* **2019**, *10*, 1702–1708.
- (30) Yu, C.-J.; von Kugelgen, S.; Krzyaniak, M. D.; Ji, W.; Dichtel, W. R.; Wasielewski, M. R.; Freedman, D. E. Spin and phonon design in modular arrays of molecular qubits. *Chem. Mater.* **2020**, *32*, 10200–10206.
- (31) Eaton, S. S.; Eaton, G. R. Relaxation Mechanisms. In *EPR Spectroscopy: Fundamentals and Methods*; Goldfarb, D., Stoll, S., Eds.; John Wiley & Sons: 2018; pp 175–192.
- (32) Amdur, M. J.; Mullin, K. R.; Waters, M. J.; Puggioni, D.; Wojnar, M. K.; Gu, M.; Sun, L.; Oyala, P. H.; Rondinelli, J. M.; Freedman, D. E. Chemical control of spin–lattice relaxation to discover a room temperature molecular qubit. *Chem. Sci.* **2022**, *13*, 7034–7045.
- (33) Dai, Y.-Z.; Dong, B.-W.; Kao, Y.; Wang, Z.-Y.; Un, H.-I.; Liu, Z.; Lin, Z.-J.; Li, L.; Xie, F.-B.; Lu, Y.; Xu, M.-X.; Lei, T.; Sun, Y.-J.; Wang, Y.; Gao, S.; Jiang, S.-D.; Pei, J. Chemical modification toward long spin lifetimes in organic conjugated radicals. *ChemPhysChem* **2018**, *19*, 2972–2977.
- (34) Haugland, M. M.; Lovett, J. E.; Anderson, E. A. Advances in the synthesis of nitroxide radicals for use in biomolecule spin labelling. *Chem. Soc. Rev.* **2018**, *47*, 668–680.
- (35) Thankamony, A. S. L.; Wittmann, J. J.; Kaushik, M.; Corzilius, B. Dynamic nuclear polarization for sensitivity enhancement in modern solid-state NMR. *Prog. Nucl. Mag. Res. Sp.* **2017**, *102*, 120–195.
- (36) Zhang, T.; Pramanik, G.; Zhang, K.; Gulka, M.; Wang, L.; Jing, J.; Xu, F.; Li, Z.; Wei, Q.; Cigler, P.; Chu, Z. Toward quantitative bio-
- sensing with nitrogen–vacancy center in diamond. *ACS Sens.* **2021**, *6*, 2077–2107.
- (37) Doorslaer, S. V. Hyperfine Spectroscopy – ESEEM. In *EPR Spectroscopy: Fundamentals and Methods*; Goldfarb, D., Stoll, S., Eds.; John Wiley & Sons: 2018; pp 377–400.
- (38) Zhou, H.-C.; Long, J. R.; Yaghi, O. M. Introduction to metal–organic frameworks. *Chem. Rev.* **2012**, *112*, 673–674.
- (39) Li, H.-Y.; Zhao, S.-N.; Zang, S.-Q.; Li, J. Functional metal–organic frameworks as effective sensors of gases and volatile compounds. *Chem. Soc. Rev.* **2020**, *49*, 6364–6401.
- (40) Koo, W.-T.; Jang, J.-S.; Kim, I.-D. Metal–organic Frameworks for chemiresistive sensors. *Chem* **2019**, *5*, 1938–1963.
- (41) Marquis, S.; Moissette, A.; Vezin, H.; Brémard, C. Long-lived radical cation–electron pairs generated by anthracene sorption in non Brønsted acidic zeolites. *J. Phys. Chem. B* **2005**, *109*, 3723–3726.
- (42) Moissette, A.; Marquis, S.; Cornu, D.; Vezin, H.; Brémard, C. Long-lived spin-correlated pairs generated by photolysis of naphthalene occluded in non-Brønsted acidic ZSM-5 zeolites. *J. Am. Chem. Soc.* **2005**, *127*, 15417–15428.
- (43) Kultraeva, A.; Pöpl, A.; Biktagirov, T. Atomic-scale quantum sensing of ensembles of guest molecules in a metal–organic framework with intrinsic electron spin centers. *J. Phys. Chem. Lett.* **2022**, *13*, 6737–6742.
- (44) Hmadeh, M.; Lu, Z.; Liu, Z.; Gándara, F.; Furukawa, H.; Wan, S.; Augustyn, V.; Chang, R.; Liao, L.; Zhou, F.; Perre, E.; Ozolins, V.; Suenaga, K.; Duan, X.; Dunn, B.; Yamamoto, Y.; Terasaki, O.; Yaghi, O. M. New porous crystals of extended metal–catecholates. *Chem. Mater.* **2012**, *24*, 3511–3513.
- (45) Naidek, K. P.; Zuconelli, C. R.; Cruz, O. M.; Ribeiro, R.; Winnischofer, S. M. B.; Winnischofer, H. Characterization of 2,3,6,7,10,11-hexahydroxytriphenylene and its effects on cell viability in human cancer cell lines. *Biochem. Cell Biol.* **2016**, *94*, 205–211.
- (46) Misumi, Y.; Yamaguchi, A.; Zhang, Z.; Matsushita, T.; Wada, N.; Tsuchiizu, M.; Awaga, K. Quantum spin liquid state in a two-dimensional semiconductive metal–organic framework. *J. Am. Chem. Soc.* **2020**, *142*, 16513–16517.
- (47) Dou, J.-H.; Arguilla, M. Q.; Luo, Y.; Li, J.; Zhang, W.; Sun, L.; Mancuso, J. L.; Yang, L.; Chen, T.; Parent, L. R.; Skorupskii, G.; Libretto, N. J.; Sun, C.; Yang, M. C.; Dip, P. V.; Brignole, E. J.; Miller, J. T.; Kong, J.; Hendon, C. H.; Sun, J.; Dincă, M. Atomically precise single-crystal structures of electrically conducting 2D metal–organic frameworks. *Nat. Mater.* **2021**, *20*, 222–228.
- (48) Huang, Z.; Grape, E. S.; Li, J.; Inge, A. K.; Zou, X. 3D electron diffraction as an important technique for structure elucidation of metal–organic frameworks and covalent organic frameworks. *Coord. Chem. Rev.* **2021**, *427*, 213583.
- (49) Grange, C. S.; Meijer, A. J. H. M.; Ward, M. D. Trinuclear ruthenium dioxolane complexes based on bridging ligand hexahydroxytriphenylene: electrochemistry, spectroscopy, and near-infrared electrochromic behaviour associated with a reversible seven-membered redox chain. *Dalton Trans.* **2010**, *39*, 200–211.
- (50) Skorupskii, G.; Le, K. N.; Cordova, D. L. M.; Yang, L.; Chen, T.; Hendon, C. H.; Arguilla, M. Q.; Dincă, M. Porous lanthanide metal–organic frameworks with metallic conductivity. *Proc. Natl. Acad. Sci. U. S. A.* **2022**, *119*, e2205127119.
- (51) Stoll, S. Pulse EPR. In *EPR Spectroscopy: Fundamentals and Methods*; Goldfarb, D., Stoll, S., Eds.; John Wiley & Sons: 2018; pp 215–233.
- (52) Hu, Y.; Teat, S. J.; Gong, W.; Zhou, Z.; Jin, Y.; Chen, H.; Wu, J.; Cui, Y.; Jiang, T.; Cheng, X.; Zhang, W. Single crystals of mechanically entwined helical covalent polymers. *Nat. Chem.* **2021**, *13*, 660–665.
- (53) Wang, B.; Le Fevre, L. W.; Brookfield, A.; McInnes, E. J. L.; Dryfe, R. A. W. Resolution of lithium deposition versus intercalation of graphite anodes in lithium ion batteries: an in situ electron paramagnetic resonance study. *Angew. Chem., Int. Ed.* **2021**, *60*, 21860–21867.



(54) Cao, D.; Lan, J.; Wang, W.; Smit, B. Lithium-doped 3D covalent organic frameworks: high-capacity hydrogen storage materials. *Angew. Chem., Int. Ed.* **2009**, *48*, 4730–4733.

(55) Downard, A.; Nieuwenhuyzen, M.; Seddon, K. R.; van den Berg, J.-A.; et al. Structural features of lithium organoborates. *Cryst. Growth Des.* **2002**, *2*, 111–119.

(56) Chang, H.-C.; Mochizuki, K.; Kitagawa, S. Effects of countercations on the structures and redox and spectroscopic properties of diruthenium catecholate complexes with ligand-unsupported Ru–Ru bonds. *Inorg. Chem.* **2005**, *44*, 3810–3817.

(57) Tyryshkin, A. M.; Dikanov, S. A.; Goldfarb, D. Sum combination harmonics in four-pulse ESEEM spectra. Study of the ligand geometry in aqua–vanadyl complexes in polycrystalline and glass matrices. *J. Magn. Reson., Ser. A* **1993**, *105*, 271–283.

(58) Milov, A. D.; Samoilova, R. I.; Shubin, A. A.; Grishin, Yu. A.; Dzuba, S. A. ESEEM measurements of local water concentration in D<sub>2</sub>O-containing spin-labeled systems. *Appl. Magn. Reson.* **2008**, *35*, 73–94.

(59) Shin, B.; Saxena, S. Substantial contribution of the two imidazole rings of the His13–His14 dyad to Cu(II) binding in amyloid- $\beta$ (1–16) at physiological pH and its significance. *J. Phys. Chem. A* **2011**, *115*, 9590–9602.

(60) Langmuir, I. The adsorption of gases on plane surfaces of glass, mica and platinum. *J. Am. Chem. Soc.* **1918**, *40*, 1361–1403.

(61) Rudd, N. D.; Liu, Y.; Tan, K.; Chen, F.; Chabal, Y. J.; Li, J. Luminescent metal–organic framework for lithium harvesting applications. *ACS Sustainable Chem. Eng.* **2019**, *7*, 6561–6568.

(62) Kamenica, M.; Kothur, R. R.; Willows, A.; Patel, B. A.; Cragg, P. J. Lithium ion sensors. *Sensors* **2017**, *17*, 2430.

(63) Mitrikas, G.; Prokopiou, G. Modulation depth enhancement of ESEEM experiments using pulse trains. *J. Magn. Reson.* **2015**, *254*, 75–85.

(64) Zhou, H.; Choi, J.; Choi, S.; Landig, R.; Douglas, A. M.; Isoya, J.; Jelezko, F.; Onoda, S.; Sumiya, H.; Cappellaro, P.; Knowles, H. S.; Park, H.; Lukin, M. D. Quantum metrology with strongly interacting spin systems. *Phys. Rev. X* **2020**, *10*, No. 031003.

(65) Hu, Y.-S.; Lu, Y. The mystery of electrolyte concentration: from superhigh to ultralow. *ACS Energy Lett.* **2020**, *5*, 3633–3636.

(66) Su, J.; Xu, N.; Murase, R.; Yang, Z.-M.; D'Alessandro, D. M.; Zuo, J.-L.; Zhu, J. Persistent radical tetrathiafulvalene-based 2D metal–organic frameworks and their application in efficient photothermal conversion. *Angew. Chem., Int. Ed.* **2021**, *60*, 4789–4795.

(67) Ellison, W. J. Permittivity of pure water, at standard atmospheric pressure, over the frequency range 0–25 THz and the temperature range 0–100 °C. *J. Phys. Chem. Ref. Data* **2007**, *36*, 1–18.

(68) Zhang, X.; Wolf, C.; Wang, Y.; Aubin, H.; Bilgeri, T.; Willke, P.; Heinrich, A. J.; Choi, T. Electron spin resonance of single iron phthalocyanine molecules and role of their non-localized spins in magnetic interactions. *Nat. Chem.* **2022**, *14*, 59–65.